Chapter 6:

Mixed-dimensional excitons in SnS/BNNT heterostructure

6.1 Introduction

Heterostructures offer a strategic platform for combining the unique properties of different materials to achieve enhanced or novel functionalities [1–6]. With the rapid expansion of van der Waals (vdW) layered materials, researchers now have unprecedented opportunities to engineer 2D/2D heterostructures that integrate diverse material families with distinct electronic, optical, and structural characteristics [7–11]. These vdW heterostructures often exhibit synergistic properties, which are not possessed by the conventional material.

Importantly, vdW interactions are not confined to interplanar forces in layered materials [12]. Any passivated, dangling-bond-free surface can engage in vdW bonding, enabling 2D materials to form heterostructures with materials of varying dimensionalities. This fundamental property allows layered 2D materials to be integrated with a wide range of materials of different dimensionalities, giving rise to mixed-dimensional vdW heterostructures. These combinations, involving 2D + nD (where n = 0, 1, or 3) materials, have emerged as a broad and versatile class of heterostructures, opening new avenues for material design and multifunctional applications [12–15]. 2D/1D and 2D/0D vdW systems are particularly compelling because they merge the quantum confinement effects of lower-dimensional components with the excellent in-plane charge transport characteristics of 2D materials.

A key phenomenon in vdW heterostructures is the formation of interfacial excitons (IFEs), which are bound electron-hole pairs with the electron and hole spatially located in adjacent layers [9,16–18]. In type-II band-aligned heterostructures, this spatial separation reduces the overlap of electron-hole wave functions, improving exciton lifetimes ($\sim 10^{-6}$ s) and allows for tunable binding energies [19]. IFEs are typically observed in 2D/2D vdW systems, where both charge carriers experience similar confinement effects and reduced dimensional screening.

In mixed-dimensional heterostructures, however, IFEs acquire a new level of complexity. Since the electron and hole are confined in materials of different dimensionalities (e.g., 2D/1D), the resulting excitons, termed as ‘inter-dimensional excitons (IDE)’, experience asymmetric confinement and dimension-dependent screening effects. One charge carrier may reside in a more confined lattice, leading to discretized energy states and modified Coulombic interactions. Understanding these effects are crucial, as such interdimensional excitons could enable unique excitonic behaviours and improved light-matter coupling, opening new directions for efficient energy-harvesting and quantum optoelectronic devices.

In the previous chapter, we examined the optoelectronic properties of a 2D/2D mixed-phase SnS/*h*-BN heterostructure under the influence of a built-in intralayer electric field. Over the past few years, considerable efforts have been directed toward exploring various 2D/2D SnS-based heterostructures, such as, SnS/GeSe [9], SnS/SnSe [20], SnS/ZnS, SnS/ZnSe [21], SnS/TaS_2 [22], SnS/SnS_2 [23], SnS/$CsPbI_3$ [24], and SnS/TiO_2 [25], to tailor and enhance their optoelectronic properties. Despite this progress, heterostructures combining SnS with materials of different dimensionalities remain largely unexplored. The influence of asymmetric confinement and dimensional mismatch on excitonic behaviour, especially interfacial excitons, is not well understood and represents a significant opportunity for further research.

In this chapter, we propose a novel mixed-dimensional vdW heterostructure by stacking a monolayer of 2D SnS with a 1D boron nitride nanotube (BNNT). In the previous chapter, discussing a 2D/2D SnS/*h*-BN heterostructure, we demonstrated that integrating an anisotropic material (SnS) with an isotropic one (*h*-BN) can significantly reduce the binding energy of SnS-bound excitons via the intrinsic interfacial charge dynamics [10]. While 2D boron nitride possesses a wide band gap (~7.43 eV - 7.66 eV) [26,27] and forms a type-I band alignment when stacked with SnS [10], BNNTs offer additional tunability. Their band gaps can be adjusted by varying the nanotube diameter or chirality (n,0) [27], providing a means to potentially engineer the nature of band alignment within the mixed-dimensional heterostructure. This combination offers a promising platform for investigating inter-dimensional excitons and unlocking their potential for next-generation optoelectronic and energy-harvesting applications.

6.2 Computational details

The calculations were done using the PWSCF code in the Quantum Espresso software suite based on DFT and plane-wave pseudopotential approach [28–31]. The generalized-gradient-approximation (GGA) with non-empirical Perdew-Burke-Ernzerhof (PBE) parameterization was used to treat the exchange-correlation functional in the calculations [32]. The electron-ion interactions were modelled using the scalar-relativistic Optimized

Norm-Conserving Vanderbilt Pseudopotential (ONCVPSP) [33]. The kinetic energy cutoff (ecutwfc) and the charge density cutoff (ecutrho) for the wavefunctions was kept at 50 Ry (680 eV), and 300 Ry (4081 eV), respectively. The sampling of the primary Brillouin zone (BZ) for BNNT, monolayer SnS, SnS/BNNT heterostructures were done at 1×6×1, 6×6×1, 6×6×1 *k*-point grid, respectively generated via the Monkhorst-Pack scheme. For a precise integration of the BZ during the non-self-consistent calculations, an even denser corresponding *k*-grid of 1×18×1, 12×12×1, 12×12×1, were considered for the three structures respectively. An energy convergence threshold of 10^{-4} Ry and a force convergence threshold of 10^{-3} Ry/Bohr were used to relax the lattice and atomic parameters. The convergence criteria for self-consistent calculation were set at 10^{-8} Ry. Semi-empirical Grimme's DFT-D2 parameter accounts for the vdW force in the heterostructure [34].

Lattice mismatch along the direction of the nanotube axis was calculated by,

$$\frac{\mathrm{L_{SnS}}-\mathrm{L_{BNNT}}}{\mathrm{L_{SnS}}} \times 100 \qquad \ldots(6.1)$$

here, $\mathrm{L_{SnS}}$ and $\mathrm{L_{BNNT}}$ are the lattice parameters of SnS supercell and BNNT unit cell along *y*-direction.

The interface binding energy ($\mathrm{E_b}$) per unit cell of the heterostructure was calculated by the following formula:

$$E_{\mathrm{b}} = E_{\mathrm{SnS/BNNT}} - E_{\mathrm{SnS}} - E_{\mathrm{BNNT}} \qquad \ldots(6.2)$$

the terms $E_{\mathrm{SnS/BNNT}}$, E_{SnS}, E_{BNNT} represent the total energies of the SnS/BNNT heterostructure, isolated SnS layer, and BNNT, respectively.

The equation to calculate the charge density difference (CDD) is as follows:

$$\triangle\rho = \rho_{\mathrm{SnS/BNNT}} - \rho_{\mathrm{SnS}} - \rho_{\mathrm{BNNT}} \qquad \ldots(6.3)$$

where, $\rho_{\mathrm{SnS/BNNT}}$, ρ_{SnS}, ρ_{BNNT} indicate the overall charge densities of the SnS/BNNT heterostructure, isolated SnS layer, and BNNT, respectively.

Beyond DFT, the energy levels were corrected by introducing quasiparticle interactions through GW computations based on MBPT. The quasiparticle interaction is introduced by the following non-linear equation,

$$E_{nk}^{QP} = \epsilon_{nk} + Z_{nk} < \Psi_{nk}|\Sigma\left(E_{nk}^{QP}\right) - V_{xc}|\Psi_{nk} > \qquad \ldots(6.4)$$

where the term Z_{nk} represents renormalisation factor. With the evaluation of the dynamical and static components in the self-energy (Σ), the plasmon-pole approximation (PPA) is used to determine the single pole function frequency subjected to the dielectric matrix [35,36].

The excitonic electron-hole effect is incorporated by solving the Bethe-Salpeter Equation (BSE) [36,37],

$$(E_{ck} - E_{vk})A_{vck}^{S} + \sum\nolimits_{kv'c'} < vck|K^{eh}\,|v'c'k' > A_{v'c'k'}^{S} = \Omega^{s} A_{vck}^{S} \qquad \ldots(6.5)$$

where, the screened interaction between excited electrons and holes are described by the kernel term K^{eh} [36,37]. The terms A_{vck}^{S}, and Ω^{s} represent the electron-hole amplitudes, and the exciton energy, respectively. E_{ck} and E_{vk} are the quasiparticle energies of the electron and hole states. The subscripts v, c, and k represents the valence band (VB), conduction band (CB), and k vector, respectively. The GW+BSE computation is done using the YAMBO package [38,39].

6.3 Construction, optimization, and interfacial charge dynamics

To model the heterostructure, we first optimized the structural parameters of the SnS monolayer to its ground-state energy. The relaxed lattice constants of the monolayer are *a* = 4.05 Å and *b* = 4.43 Å, corresponding to the zigzag and armchair directions, respectively.

Table 6.1: Structural parameters, electronic band gap (E_g^{GGA} and E_g^{GW}), exciton peaks, and exciton binding energies (EBE) of SnS monolayer and zigzag BNNTs.

	Lattice parameters (Å)	**Diameter (Å)**	**E_g^{GGA} (eV)**	**E_g^{GW} (eV)**	**Exciton peaks (eV)**	**EBE (eV)**
SnS	4.05 (a), 4.43 (b)	--	1.52*	2.28*	2.50, 2.83	0.33, 0.31
BNNT						
(5,0)	4.35 (b)	4.21	2.15	6.90	5.05	1.85
(6,0)	4.36 (b)	5.01	2.77	7.35	5.35	2.00
(7,0)	4.38 (b)	5.73	3.34	7.86	5.85	2.01

* Indicates indirect band gap.

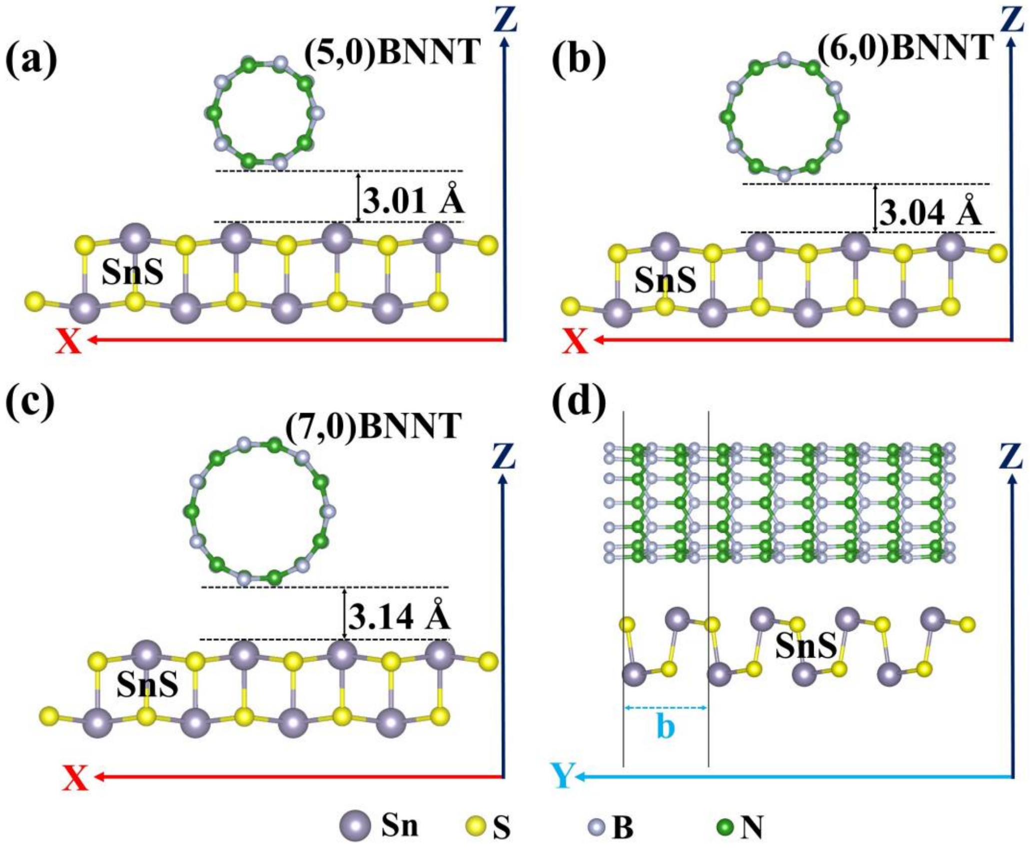

Figure 6.1: *Relaxed atomic structures of the SnS/BNNT mixed-dimensional heterostructures for three different BNNT chiralities: (a) SnS/(5,0) BNNT, (b) SnS/(6,0) BNNT, and (c) SnS/(7,0) BNNT. Panel (d) illustrates the stacking orientation, where the BNNT axis is aligned along the armchair direction of the SnS monolayer.*

These values are in good agreement with previous reports [10,40]. For constructing the mixed-dimensional heterostructure, we considered three zigzag BNNTs with chiralities (*n,0*) where *n* = 5, 6, and 7, with the tube axis aligned along the *y*-axis. The selection of low chirality was motivated by the anticipated strong curvature effects on the optical properties [27,41,42]. The optimized diameters of the (5,0), (6,0), and (7,0) BNNTs are 4.21 Å, 5.01 Å, and 5.73 Å, respectively. The corresponding lattice constants along the tube axis are *b* = 4.35 Å, 4.36 Å, and 4.38 Å. These results, along with those of the pristine SnS monolayer and BNNTs, are summarized in Table 6.1 and are consistent with earlier theoretical prediction [27,42].

The three heterostructures were constructed by stacking a single unit cell of each BNNT onto a 4×1 supercell of the SnS monolayer, as illustrated in Fig. 6.1(a-c). To minimize lattice mismatch, the BNNT tube axis was aligned with the armchair direction of the SnS

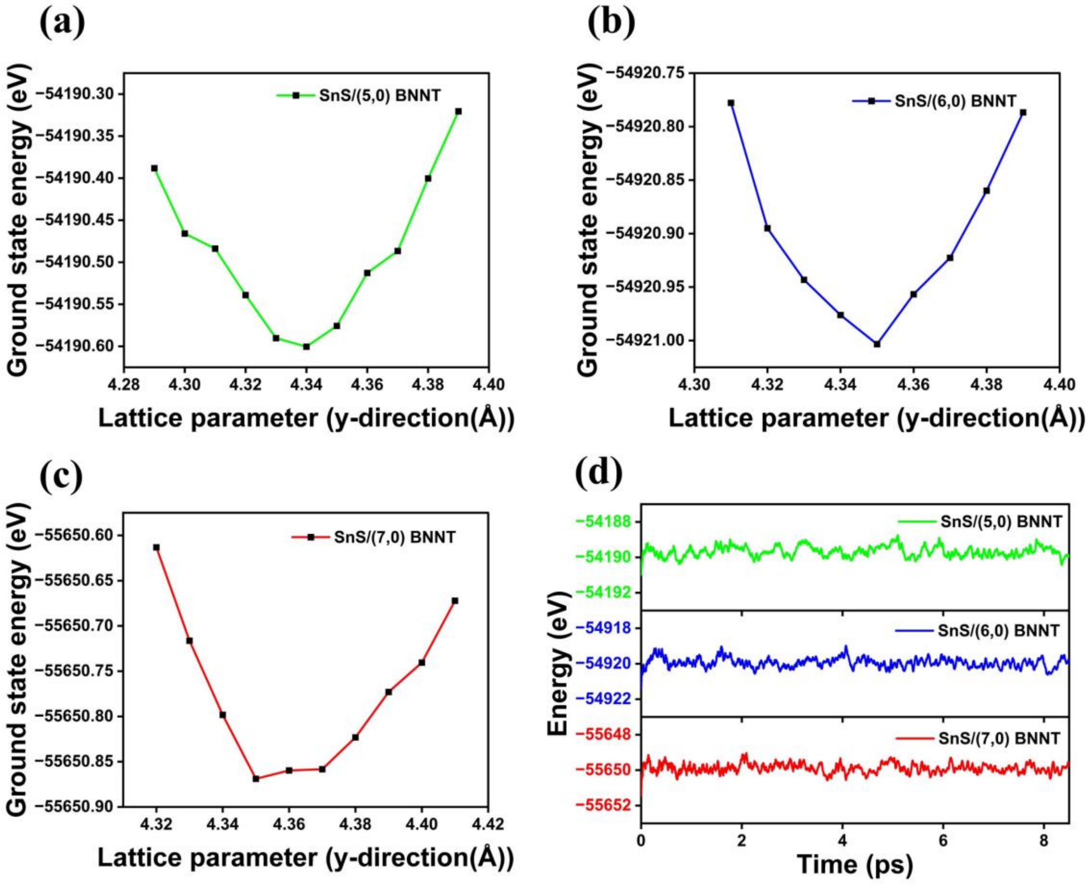

Figure 6.2: *(a-c) Convergence test for lattice parameters vs. ground state energy; (d) AIMD simulation of the SnS/BNNT heterostructures at 300 K.*

layer (Fig. 6.1(d)). The optimized lattice parameters of SnS/(5,0), SnS/(6,0), and SnS/(7,0) BNNTs are found to be 4.34 Å, 4.35 Å, and 4.35 Å, with corresponding lattice mismatches of 1.81%, 1.58%, and 1.10%, respectively (Fig. 6.2(a-c)). Such small mismatches are favourable for the thermodynamic formation of heterojunctions with minimal structural defects [43]. Moreover, the minimal energy fluctuations over a time period of 8.5 ps at room temperature indicates to the thermal stability of the heterostructures (Fig. 6.2(d)). To eliminate spurious interactions due to periodic boundary conditions, a vacuum spacing of more than 16 Å was introduced along the out-of-plane direction. Additionally, the large 4×1 supercell created more than 10 Å spacing between the in-plane parallel BNNT along the *x*-direction. The interfacial binding energies for SnS/(5,0) BNNT, SnS/(6,0) BNNT, and SnS/(7,0) BNNT heterostructures were calculated to be -0.55 eV, -0.56 eV, and -0.59 eV, respectively, indicating energetically favourable heterointerface formation.

As the chirality of the BNNT increases, the interfacial separation between the BNNT and the SnS monolayer also increases gradually, as illustrated in Fig. 6.1(a-c). The interfacial

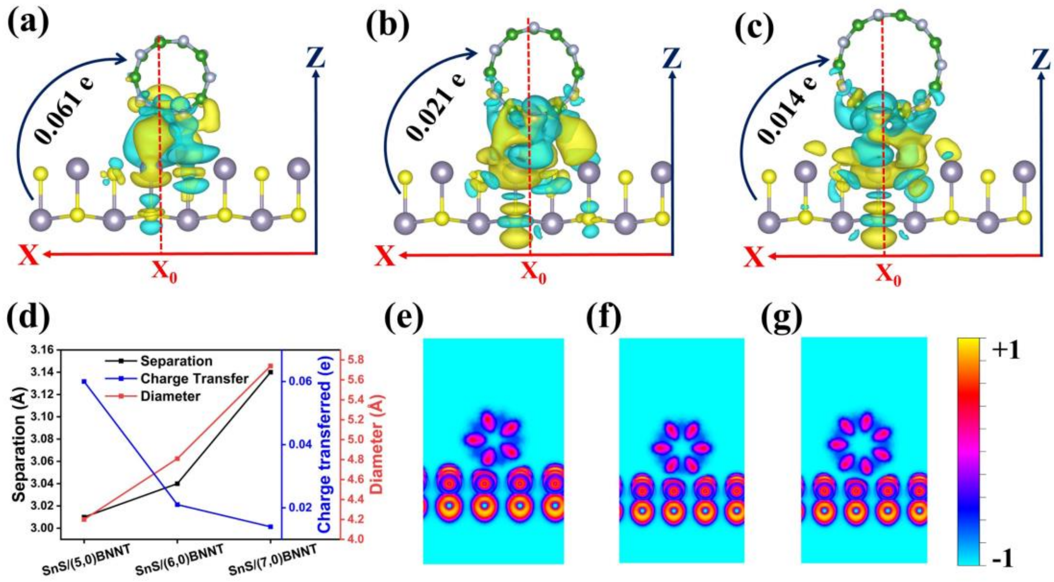

Figure 6.3: *Charge density difference (CDD) plots of the mixed-dimensional heterostructures: (a) SnS/(5,0) BNNT, (b) SnS/(6,0) BNNT, and (c) SnS/(7,0) BNNT. Cyan and yellow regions indicate charge accumulation and depletion, respectively. The point* x_0 *along the x-axis marks the location of minimum interfacial separation. (d) Variation of interfacial separation, charge transfer, and BNNT diameter as a function of increasing chirality. Electron localization function (ELF) profiles for SnS/(n,0) BNNT heterostructures are shown in (e) n = 5, (f) n = 6, and (g) n = 7, confirming the van der Waals nature of interfacial interactions (the blue to yellow colour bar indicates the lowest (-1) to highest value (+1)).*

charge dynamics of the heterostructures are shown in Fig. 6.3(a-c). Due to curvature-induced effects, charge accumulation and depletion are localized near a central region (denoted as x_0), where the vertical separation between the two materials is minimal. The amount of charge transferred from the SnS surface to the BNNT decreases with increasing BNNT diameter and interfacial distance, as shown in Fig. 6.3(d). The van der Waals nature of the interfacial interactions is confirmed by the electron localization function (ELF) plots in Fig. 6.3(e-g), indicated by the absence of significant covalent bonding at the interface.

The planar-averaged electrostatic potential profiles, shown in Fig. 6.4, reveal that the interfacial potential difference (ΔV_{hetero}) is a function of nanotube chirality. Additionally, a small intrinsic intralayer potential difference (ΔV_{SnS}) exists between the two atomic layers of the SnS monolayer, on the order of ~10^{-2} eV. With increasing nanotube chirality, ΔV_{hetero} gradually decreases, while ΔV_{SnS} shows a slight increase. Both parameters tend to

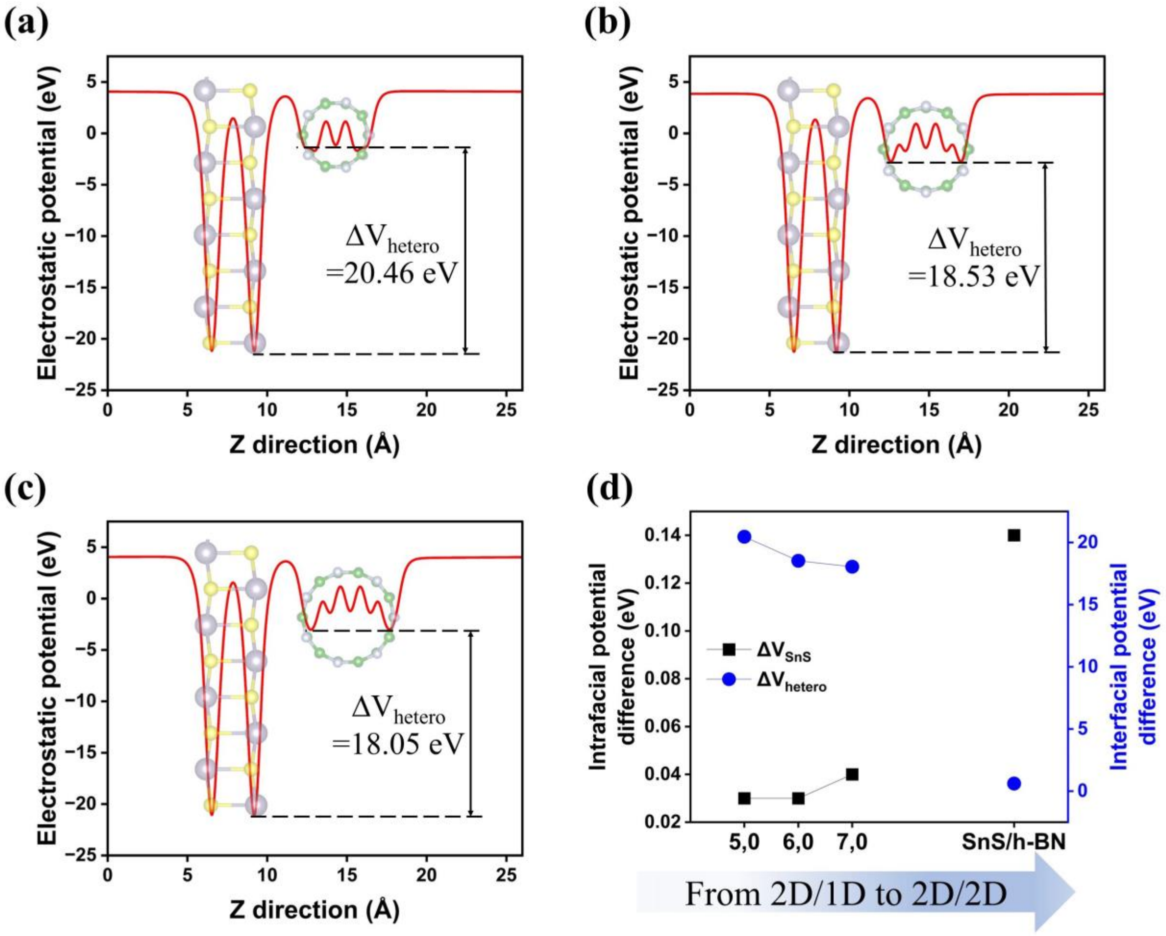

Figure 6.4: *Planar-averaged electrostatic potential profiles of the mixed-dimensional heterostructures: (a) SnS/(5,0) BNNT, (b) SnS/(6,0) BNNT, and (c) SnS/(7,0) BNNT. The evolution of the intralayer potential difference (*ΔV_{SnS}*) and interfacial potential difference (*ΔV_{hetero}*) is illustrated, highlighting the transition from 2D/1D SnS/BNNT stacking to the 2D/2D SnS/h-BN configuration.*

converge toward the values observed in a 2D/2D SnS/*h*-BN heterostructure, as depicted in Fig. 6.4(d).

6.4 DFT and quasiparticle corrected electronic structures

The electronic band structures of the three heterostructures along the high symmetric *k*-path 'X-Γ-Y-T-X' are shown in Fig. 6.5. It is important to note that the charge carriers in the SnS monolayer can propagate along both in-plane directions, whereas in the BNNT, carrier mobility is confined to a single direction, specifically along the nanotube axis (*y*-direction in this case). Consequently, the BNNT dominated bands along the X-Γ direction exhibit minimal dispersion and appear as flat bands due to this restricted mobility. Fig.

6.5(a-c) shows the structure projected band structure at the DFT-GGA level of theory. The heterostructures with the smaller nanotube chiralities i.e., *n* = 5, 6, exhibit an indirect type-II (staggered) band alignment (Fig. 6.5(a,b)). In these configurations, the valence band maximum (VBM) originates from the SnS layer, while the conduction band minimum (CBM) is dominated by the BNNT. The VBM in both heterostructures lies at the Y^* point along the Γ-Y path in the BZ, whereas the CBM spans the entire Γ-X valley due to the flat band nature. The indirect band gaps of the SnS/(5,0) BNNT and SnS/(6,0) BNNT systems are calculated to be 0.92 eV and 1.33 eV, respectively. As the chirality of the BNNT increases, the BNNT derived conduction bands shift away from the Fermi level. This shift is attributed to the diameter dependent band structure of pristine BNNTs, where the band gap widens as a function of chirality (see Table 6.1 and Appendix A.8). As a result, in the SnS/(7,0) BNNT heterostructure, the CBM is no longer contributed by the BNNT but instead originates from the SnS layer and is located at the X^* point along the X-Γ path (Fig. 6.5(c)). The VBM remains at Y^*, yielding an indirect band gap of 1.50 eV. Therefore, the DFT-GGA calculations suggest a transition in band alignment from type-II to type-I (straddling) as the BNNT chirality increases. The corresponding values of direct and indirect band gaps for all heterostructures are summarized in Table 6.2.

Table 6.2: Direct and indirect electronic band gaps of the heterostructures along with their direction/position in the momentum space at DFT-GGA ($E_\mathrm{g}^\mathrm{GGA}$) and GW ($E_\mathrm{g}^\mathrm{GW}$) level of calculation.

Nature of gap	Calculation level	Direction/ Position	SnS/(5,0) BNNT	SnS/(6,0) BNNT	SnS/(7,0) BNNT
Indirect (eV)	$E_\mathrm{g}^\mathrm{GGA}$	$\mathrm{Y}^*_\mathrm{VBM}$-$\mathrm{X}^*_\mathrm{CBM}$	0.92$^{\#}$	1.33$^{\#}$	1.50
	E_g^GW	$\mathrm{Y}^*_\mathrm{VBM}$-$\mathrm{X}^*_\mathrm{CBM}$	2.91	2.99	3.10
Direct (eV)	$E_\mathrm{g}^\mathrm{GGA}$	Y*	1.62	1.60	1.59
		X*	1.14	1.50	1.73
		Γ	1.10	1.56	1.86
	E_g^GW	Y*	3.00	3.09	3.18
		X*	3.35	3.43	3.52
		Γ	3.39	3.58	3.70

$^{\#}$ Indicates that the CBM lies at all the points of the X-Γ direction (i.e., $\mathrm{Y}^*_\mathrm{VBM}$-X$\Gamma_{CBM}$).

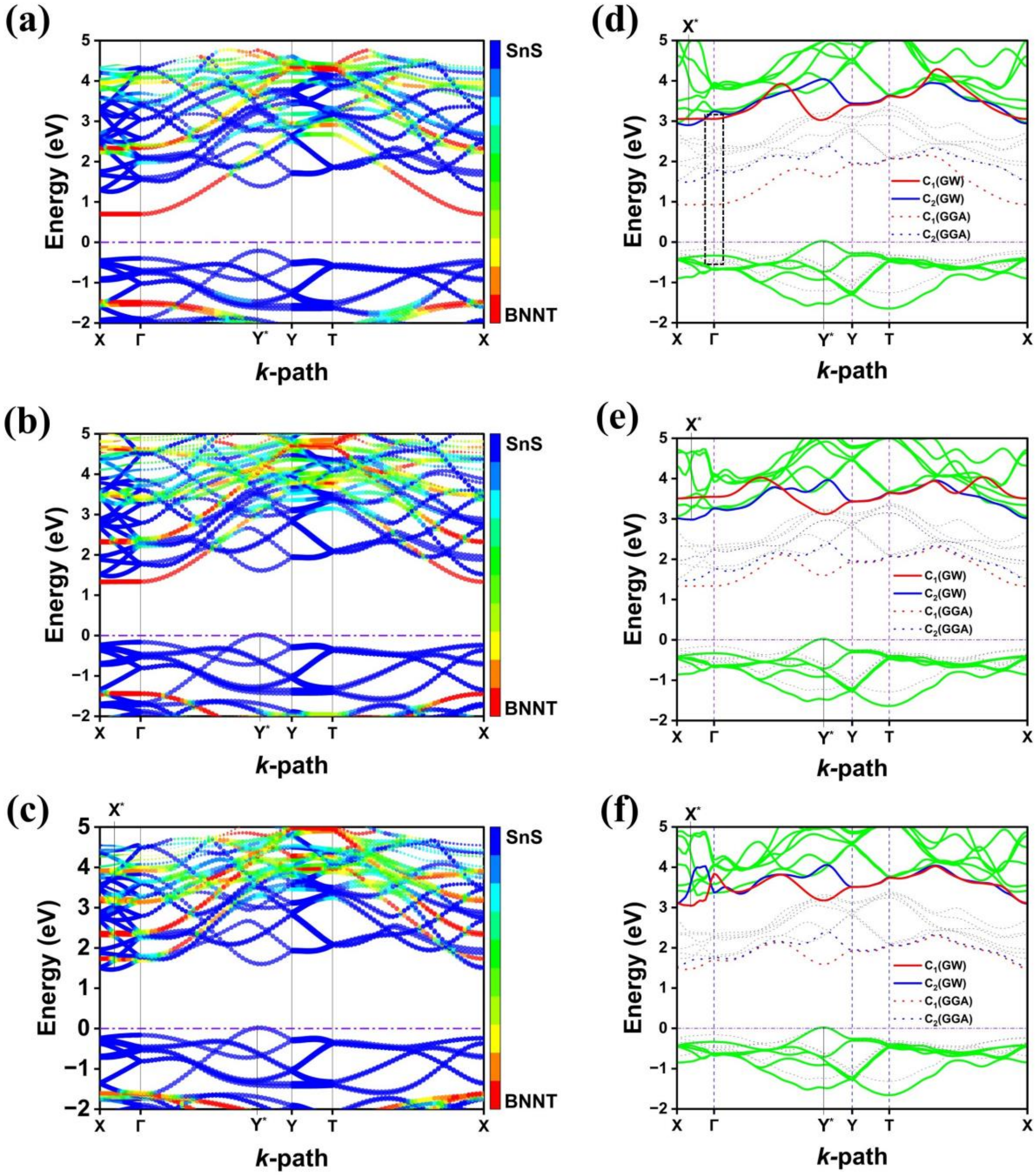

Figure 6.5: *Structure-projected electronic band structures of (a) SnS/(5,0) BNNT, (b) SnS/(6,0) BNNT, and (c) SnS/(7,0) BNNT heterostructures at the DFT-GGA level of theory. Blue and red colours represent the contributions from SnS and BNNT, respectively. The corresponding quasiparticle-corrected GW band structures are presented in (d-f), with solid lines indicating GW bands and dotted lines denoting DFT-GGA bands for comparison. To illustrate the evolution of the lower conduction bands under GW corrections, the two lowest conduction bands (C_1 and C_2) are highlighted in red and blue, respectively.*

However, it is well known that DFT-GGA calculations tend to underestimate band gaps due to the absence of many-body effects, such as electron-electron and electron-ion interactions. This can also lead to inaccurate predictions of band alignment, especially in systems involving boron nitride [26,44]. To address these limitations, we performed quasiparticle corrected GW calculations to obtain more accurate electronic structures. The GW band structures of SnS/(5,0) BNNT, SnS/(6,0) BNNT, and SnS/(7,0) BNNT heterostructures are shown in Fig. 6.5(d-f), with the corresponding DFT-GGA bands drawn as dotted lines for comparison. For simplicity, the two lowest conduction bands from the GW and GGA calculations are highlighted in red and blue, and are labelled as C_1 and C_2, respectively. As shown in Table 6.1 and Appendix A.8, quasiparticle corrections significantly widen the DFT-predicted band gaps of pristine BNNTs. Since the lowest conduction bands in the heterostructures with smaller chiralities (n = 5, 6) exhibit substantial contributions from the BNNT, it is crucial to understand the nature and evolution of these BNNT derived bands within the heterostructure, particularly after applying GW corrections.

As expected, after incorporating quasiparticle correction in SnS/(5,0) BNNT heterostructure, the C_1 band crosses the C_2, band shifting deeper into the CB along the X-Γ direction, and thus the CBM of the heterostructure is now contributed by SnS bound dispersive band at the X^* point, resulting in a type-I band alignment with an indirect band gap of 2.91 eV (Fig. 6.5(d)). However, near the Γ point of the BZ, the C_1 remains the lowest CB (indicated by the dotted box in Fig. 6.5(d)). From the structure projected band structure of SnS/(5,0) BNNT, it is clear that along the X-Γ path, the C_1 band is mostly contributed by 1D BNNT orbitals, while the highest VB are dominated by 2D SnS orbitals (Fig. 6.5(a)). This leads to a localised type-II direct band gap alignment near the Γ point, suggesting the possibility of interdimensional electron-hole pair generation under excitation (*discussed in Section 6.5*). Similar shifting of C_1 band is also observed in the GW band structure of SnS/(6,0) BNNT, but in a higher magnitude (Fig. 6.5(e)). The whole C_1 band along the X-Γ path crosses the C_2 band. As a result, the CBM lies on the C_2 band at the X^* point in the X-Γ direction, and is contributed by SnS orbitals. In contrast, for the SnS/(7,0) BNNT heterostructure, no such C_1-C_2 band crossing is observed, as the lowest conduction bands in this case are exclusively contributed by SnS (Fig. 6.5(c,f)). Thus, the heterostructures with higher BNNT chiralities (n = 6 and 7) exhibit purely type-I band alignment along the entire high-symmetry path, while partial type-II characteristic is observed only in the SnS/(5,0) BNNT system. The direct and indirect band gaps obtained from the GW calculations for all three heterostructures are summarized in Table 6.2.

6.5 Excitons across dimensional boundaries: IDE

After incorporating many-body interactions via quasiparticle corrections, the BSE was solved to obtain the band-to-band direct optical transitions in the SnS/BNNT heterostructures. The imaginary part of the macroscopic dielectric function, Im (ε), for linearly polarized light along the in-plane x- and y-directions is shown in Fig. 6.6(a-c). Vertical drop lines indicate the strength of the excitonic transitions, normalized on a scale from 0 to 1 (refer to the right axis in each panel). To assess excitonic effects, we calculated the optical absorption spectra both with (w/eh) and without (wo/eh) electron-hole interactions. At the GW level of theory, all heterostructures exhibit type-I direct band gaps dominated by SnS states along the Γ-X and Γ-Y valleys (Fig. 6.5 and Table 6.2). Consequently, the first two excitonic peaks, labelled A_{SnS} and B_{SnS}, correspond to intralayer excitons localized within the SnS monolayer.

As summarized in Table 6.3 and illustrated in Fig. 6.6(a-c), all SnS/BNNT heterostructures exhibit a notable blue shift in the A_{SnS} and B_{SnS} excitonic peaks, along with enhanced exciton binding energies (EBEs), compared to pristine monolayer SnS. This blue shift becomes more prominent with higher BNNT chirality. As the diameter (chirality) of the BNNT increases, the band gap becomes broader, which significantly affects the dispersion of the SnS-derived bands. This reduced band dispersion limits charge carrier mobility, leading to higher EBEs in A_{SnS} and B_{SnS}, and causing a blue shift in the excitonic feature.

Table 6.3: Excitonic peak positions and EBEs for the A_{SnS} (Γ-Y) and B_{SnS} (Γ-X) excitons, along with the corresponding direct band gaps of the three SnS/BNNT heterostructures. For reference, the values for the pristine SnS monolayer are also included.

System	**SnS monolayer**		**SnS/(5,0) BNNT**		**SnS/(6,0) BNNT**		**SnS/(7,0) BNNT**	
k-valley	Γ-Y	Γ-X	Γ-Y	Γ-X	Γ-Y	Γ-X	Γ-Y	Γ-X
Direct band gap (eV)	2.50	2.83	3.00	3.35	3.09	3.43	3.18	3.52
Exciton peak (eV)	2.17	2.52	2.46	2.70	2.51	2.81	2.58	2.87
EBE (eV)	0.33	0.31	0.54	0.65	0.58	0.62	0.60	0.65

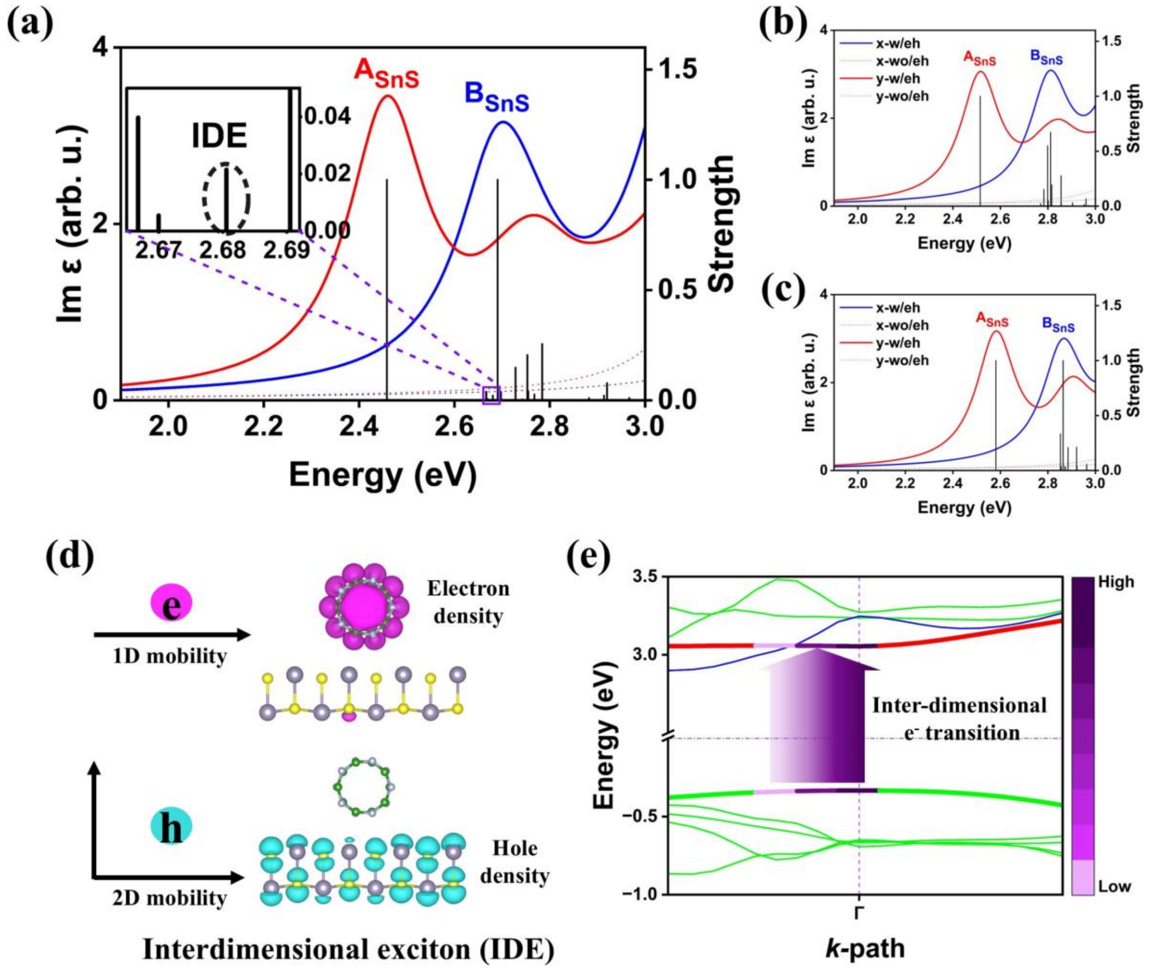

Figure 6.6: *Optical absorption spectra of (a) SnS/(5,0) BNNT, (b) SnS/(6,0) BNNT, and (c) SnS/(7,0) BNNT heterostructures. Excitonic transition strengths are indicated by vertical drop lines, normalized on a scale from 0 to 1. (d) Spatial distribution of the averaged electron-hole density associated with the interdimensional exciton (IDE) in the SnS/(5,0) BNNT heterostructure; the pink and cyan regions represent the electron and hole densities, respectively. (e) Magnified view of the GW band structure of SnS/(5,0) BNNT near the Γ-point, illustrating the momentum-space distribution and transition weight of the IDE state.*

While our analysis includes intralayer SnS bound excitons, the primary focus is to explore the generation of interdimensional electron-hole pairs near the Γ-point in the SnS/(5,0) BNNT heterostructure, due to the presence of a localized type-II direct band gap. Notably, in Fig. 6.6(a), a distinct low-energy transition state emerges at 2.68 eV (see inset), which does not correspond to the typical SnS bound intralayer transitions. This state is identified IDE, in which the excited electron is localized within the 1D BNNT, while the corresponding hole remains in the 2D SnS layer. The binding energy of this IDE is calculated to be 0.71 eV.

The spatial distribution of the electron and hole densities associated with the IDE is depicted in Fig. 6.6(d), illustrating their confinement within distinct dimensional components of the heterostructure. A magnified view of the GW band structure near the Γ-point, shown in Fig. 6.6(e), highlights the transition weights associated with the IDE. The transition weight is maximum at the Γ-point and gradually diminishes as the C_1 band intersects with C_2 along the Γ-X direction. Upon excitation, an electron transitions from the discretized, dispersive 2D VB states of SnS to the more discretized, strongly confined 1D CB states of the BNNT. This confinement results in a dispersion less (flat) C_1 band in the conduction region. Consequently, the group velocity of the electron, defined as $v_g = \frac{1}{\hbar}\frac{dE}{dK}$, approaches zero, rendering the negatively charged particle effectively immobile. This behaviour is reflected in the effective mass of the electron $m_e^* = \hbar^2 (\frac{d^2E}{dk^2})^{-1}$, which diverges as the band curvature vanishes, indicating an extremely large or practically infinite effective mass.

In contrast, the hole in the valence band does not experience such confinement and maintains a finite effective mass. As a result of the strong electron confinement, the total effective mass of the exciton, $m^* = m_e^* + m_h^*$, becomes exceptionally large. This makes the IDE a highly localized quasiparticle in real space, where the electron remains nearly static, and the hole governs the centre-of-mass dynamics. The pronounced spatial confinement of the electron-hole pair results in a large exciton binding energy.

6.6 Modulating inter-dimensional excitons via strain

From Fig. 6.6(e), we observe that the interdimensional exciton probability diminishes once C_1 crosses C_2, as the type-II direct band gap is localized near the Γ-point. As a result, only a single transition state is observed across dimensional boundaries in the unstrained case. Strain provides an effective way of further modulating the electronic band structure and excitonic properties of quantum confined materials. For example, in the SnS/GeSe 2D/2D heterostructure, strain has been effectively employed to tune both the peak position and the binding energy of the interlayer exciton [9]. In this regard, we apply uniaxial tensile and compressive strain along the nanotube axis (*y*-direction) of the SnS/(5,0) BNNT heterostructure. Fig. 6.7(a-c) presents the band structures under compressive strain levels

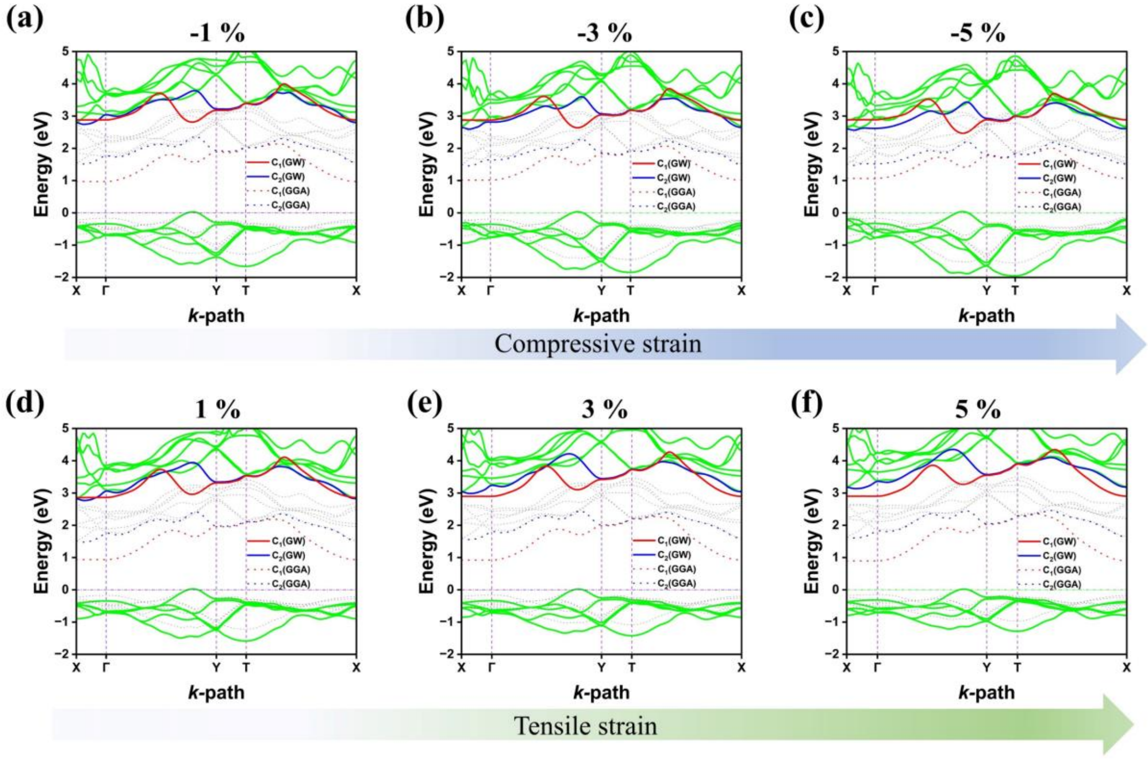

Figure 6.7: *Electronic band structures of the SnS/(5,0) BNNT heterostructure under uniaxial strain applied along the nanotube axis. Panels (a-c) show the band structures under compressive strain of -1%, -3%, and -5%, respectively, while panels (d-f) correspond to tensile strain of +1%, +3%, and +5%.*

of 1%, 3%, and 5%, respectively, while Fig. 6.7(d-f) correspond to tensile strain at the similar percentages. In all cases, the C_1 band remains intact and unchanged.

Under increasing compressive strain, the rest of the conduction band (except C_1) shift closer to the valence band, leading to a gradual reduction in the band gap. This shift eliminates the localized type-II direct gap at the Γ-point, thereby suppressing the IDE state. Conversely, with increasing tensile strain, the rest of the conduction band shifts further away from the valence band, while C_1 remains unaffected. As a result, the CBM becomes localized along the C_1 band in the whole X-Γ direction at 3% and 5% tensile strain. This marks a transition from a type-I to a type-II alignment in the SnS/(5,0) BNNT heterostructure.

Importantly, this type-II alignment under tensile strain now spans a local direct band gap along the entire Γ-X valley. Since C_1 no longer crosses C_2, the heterostructure gains access to multiple IDE transition states. While the pristine SnS/(5,0) BNNT exhibits only a single

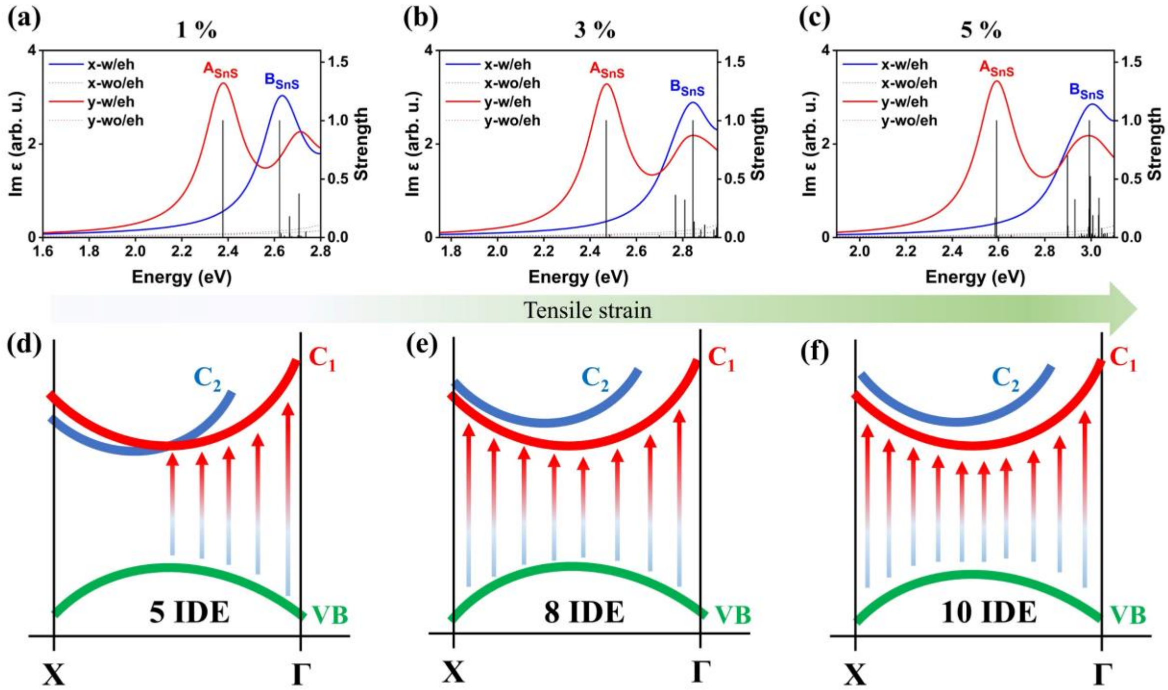

Figure 6.8: *Optical absorption spectra of the SnS/(5,0) BNNT heterostructure under uniaxial tensile strain of (a) 1%, (b) 3%, and (c) 5%. The corresponding schematic illustrations in (d-f) depict the evolution of the* C_1 *and* C_2 *conduction bands with increasing tensile strain, highlighting the increase in the number of available IDE transition states across the Γ-X valley.*

Table 6.4: Peak positions of the IDEs under tensile strain.

Strain %	IDEs energies (eV)	No. of IDEs
0 (unstrained)	2.68	1
1%	2.50, 2.56, 2.64, 2.67, 2.70	5
3%	2.48, 2.54, 2.67, 2.70, 2.74, 2.77, 2.80, 2.83	8
5%	2.00, 2.32, 2.36, 2.40, 2.43, 2.48, 2.52, 2.54, 2.57, 2.63	10

interdimensional transition state, the structure under 1%, 3%, and 5% uniaxial tensile strain displays five, eight, and ten such states, respectively. The positions of the IDE states are provided in Table 6.4. The corresponding optical absorption spectra and schematic illustrations of the increasing number of IDE transition states are shown in Fig. 6.8(a-c) and Fig. 6.8(d-f), respectively.

6.7 Conclusion

In summary, we have systematically investigated the structural, electronic, and excitonic properties of SnS/BNNT mixed-dimensional heterostructures using DFT, GW, and BSE methodologies. The study reveals that the chirality of the BNNT plays a decisive role in modulating band alignment. DFT predicts a transition from indirect type-II to type-I alignment with increasing BNNT diameter, whereas quasiparticle GW corrections show a uniform type-I alignment across all three heterostructures, with corrected indirect band gaps ranging from 2.91 eV to 3.10 eV. A key finding is the emergence of a localised type-II direct gap near the Γ-point in the SnS/(5,0) BNNT heterostructure, which enables the formation of an IDE. This IDE, characterized by a flat BNNT-derived conduction band (C_1), exhibits a transition energy of 2.68 eV and a large binding energy of 0.71 eV, resulting from the large effective mass and strong spatial confinement of the electron. Upon applying uniaxial strain along the nanotube axis, the band structure and excitonic landscape of SnS/(5,0) BNNT are further modulated. Compressive strain eliminates the localised type-II direct band alignment, suppressing IDE formation. In contrast, tensile strain enhances IDE behaviour by shifting the SnS bound conduction bands and increases the number of accessible interdimensional transitions from one (unstrained) to five, eight, and ten under 1%, 3%, and 5% tensile strain, respectively.

This work demonstrates that mixed-dimensional SnS/BNNT heterostructures are highly tunable platforms for engineering novel excitonic phenomena. The strong confinement, large binding energies, and strain-dependent tunability of IDEs make these heterostructures promising for future quantum optoelectronic applications. Importantly, this study presents a conceptual and computational framework for understanding and designing mixed-dimensional van der Waals heterostructures. The demonstration of interdimensional excitons in this system provides a foundational reference for exploring the optoelectronic properties of diverse 2D/1D material combinations.

References

[1] Zheng, H., Li, Y., Liu, H., Yin, X., Li, Y. Construction of heterostructure materials toward functionality. *Chemical Society Reviews*, 40(9): 4506–4524, 2011.

[2] Geim, A. K., Grigorieva, I. V. Van der Waals heterostructures. *Nature*, 499(7459): 419–425, 2013.

[3] Novoselov, K. S., Mishchenko, A., Carvalho, A., Castro Neto, A. H. 2D materials and van der Waals heterostructures. *Science*, 353(6298): aac9439, 2016.

[4] Pham, P. V, Bodepudi, S. C., Shehzad, K., Liu, Y., Xu, Y., Yu, B., Duan, X. 2D heterostructures for ubiquitous electronics and optoelectronics: principles, opportunities, and challenges. *Chemical reviews*, 122(6): 6514–6613, 2022.

[5] Neupane, G. P., Zhou, K., Chen, S., Yildirim, T., Zhang, P., Lu, Y. In-Plane Isotropic/Anisotropic 2D van der Waals Heterostructures for Future Devices. *Small*, 15(11): 1804733, 2019.

[6] Wang, J., Li, Z., Chen, H., Deng, G., Niu, X. Recent advances in 2D lateral heterostructures. *Nano-Micro Letters*, 11: 1–31, 2019.

[7] He, F., Zhou, Y., Ye, Z., Cho, S. H., Jeong, J., Meng, X., Wang, Y. Moiré Patterns in 2D Materials: A Review. *ACS Nano*, 15(4): 5944–5958, 2021.

[8] Li, Y., Zhang, J., Chen, Q., Xia, X., Chen, M. Emerging of heterostructure materials in energy storage: a review. *Advanced Materials*, 33(27): 2100855, 2021.

[9] Maity, N., Srivastava, P., Mishra, H., Shinde, R., Singh, A. K. Anisotropic Interlayer Exciton in GeSe/SnS van der Waals Heterostructure. *Journal of Physical Chemistry Letters*, 12(7): 1765–1771, 2021.

[10] Talukdar, D., Mohanta, D., Ahmed, G. A. Enhancing the optoelectronic properties of SnS via mixed-phase heterostructure engineering. *Nanoscale*, 17(6): 3331–3340, 2025.

[11] Kistner-Morris, J., Shi, A., Liu, E., Arp, T., Farahmand, F., Taniguchi, T., Watanabe, K., Aji, V., Lui, C.H., Gabor, N. Electric-field tunable Type-I to Type-II band alignment transition in $MoSe_2/WS_2$ heterobilayers. *Nature Communications*, 15(1): 4075, 2024.

[12] Jariwala, D., Marks, T. J., Hersam, M. C. Mixed-dimensional van der Waals heterostructures. *Nature materials*, 16(2): 170–181, 2017.

[13] Zhang, Z., Lin, P., Liao, Q., Kang, Z., Si, H., Zhang, Y. Graphene-based mixed-dimensional van der Waals heterostructures for advanced optoelectronics. *Advanced Materials*, 31(37): 1806411, 2019.

[14] Wang, P., Jia, C., Huang, Y., Duan, X. Van der Waals heterostructures by design: from 1D and 2D to 3D. *Matter*, 4(2): 552–581, 2021.

[15] Fang, N., Chang, Y.R., Yamashita, D., Fujii, S., Maruyama, M., Gao, Y., Fong, C.F., Otsuka, K., Nagashio, K., Okada, S. and Kato, Y.K. Resonant exciton transfer in mixed-dimensional heterostructures for overcoming dimensional restrictions in optical processes. *Nature communications*, 14(1): 8152, 2023.

[16] Torun, E., Miranda, H. P. C., Molina-Sánchez, A., Wirtz, L. Interlayer and intralayer excitons in MoS_2/WS_2 and $MoSe_2/WSe_2$ heterobilayers. *Physical Review B*, 97(24): 245427, 2018.

[17] Latini, S., Winther, K. T., Olsen, T., Thygesen, K. S. Interlayer Excitons and Band Alignment in MoS_2/hBN/WSe_2 van der Waals Heterostructures. *Nano Letters*, 17(2): 938–945, 2017.

[18] Jiang, Y., Chen, S., Zheng, W., Zheng, B., Pan, A. Interlayer exciton formation, relaxation, and transport in TMD van der Waals heterostructures. *Light: Science & Applications*, 10(1): 72, 2021.

[19] Zhao, S., Cheng, Y., Tao, L. Modulation and Optoelectronic Applications of van der Waals Interlayer Excitons. *ACS Photonics*, 11(7): 2529–2545, 2024.

[20] Do, T. N., Idrees, M., Amin, B., Hieu, N. N., Phuc, H. V., Hoa, L. T., Nguyen, C. V. First principles study of structural, optoelectronic and photocatalytic properties of SnS, SnSe monolayers and their van der Waals heterostructure. *Chemical Physics*, 539: 110939, 2020.

[21] Raturi, A., Mittal, P., Choudhary, S. Enhanced absorption in SnS/SnSe, SnS/ZnS, and SnS/ZnSe vdW heterostructures for optoelectronic applications: DFT insights. *Physica Scripta*, 99(12): 125508, 2024.

[22] Hassan, A., Nazir, M. A., Shen, Y., Guo, Y., Kang, W., Wang, Q. First-principles study of the structural, electronic, and enhanced optical properties of SnS/TaS_2 heterojunction. *ACS Applied Materials & Interfaces*, 14(1): 2177–2184, 2021.

[23] Cheng, Y., Tang, P., Liang, P., Liu, X., Cao, D., Chen, X., Shu, H. Sulfur-driven transition from vertical to lateral growth of 2D SnS–SnS_2 heterostructures and their

band alignments. *The Journal of Physical Chemistry C*, 124(50): 27820–27828, 2020.

[24] Cao, Y., Li, Y., He, J., Qian, C., Zhang, Q., Bai, J., Feng, H. Asymmetric Strain-Introduced Interface Effect on the Electronic and Optical Properties of the $CsPbI_3$/SnS van der Waals Heterostructure. *Advanced Materials Interfaces*, *6*(24): 1901330, 2019.

[25] Khan, M. I., Hussain, S., Alwadai, N., Fatima, M., Shahzad, U., Yousef, E. S., Iqbal, M. Heterostructure of TiO_2 and SnS for enhancing the structural, optical and photovoltaic properties of solar cells. *Optik*, *300:* 171625, 2024.

[26] Talukdar, D., Bora, S. S., Ahmed, G. A. Electronic, optical, and adsorption properties of Li-doped hexagonal boron nitride: a GW approach. *Physical Chemistry Chemical Physics*, 26(5): 4021–4028, 2024.

[27] Huang, Y. S., Chan, Y. H., Guo, G. Y. Large shift currents via in-gap and charge-neutral excitons in a monolayer and nanotubes of BN. *Physical Review B*, 108(7): 075413, 2023.

[28] Giannozzi, P., Baroni, S., Bonini, N., Calandra, M., Car, R., Cavazzoni, C., Ceresoli, D., Chiarotti, G.L., Cococcioni, M., Dabo, I., Dal Corso, A. QUANTUM ESPRESSO: a modular and open-source software project for quantum simulations of materials. *Journal of physics: Condensed matter*, 21(39): 395502, 2009.

[29] Giannozzi, P., Andreussi, O., Brumme, T., Bunau, O., Nardelli, M.B., Calandra, M., Car, R., Cavazzoni, C., Ceresoli, D., Cococcioni, M. and Colonna, N. Advanced capabilities for materials modelling with Quantum ESPRESSO. *Journal of physics: Condensed matter*, 29(46): 465901, 2017.

[30] Carnimeo, I., Affinito, F., Baroni, S., Baseggio, O., Bellentani, L., Bertossa, R., Delugas, P.D., Ruffino, F.F., Orlandini, S., Spiga, F. and Giannozzi, P. Quantum ESPRESSO: One Further Step toward the Exascale. *Journal of Chemical Theory and Computation*, 19(20): 6992–7006, 2023.

[31] Giannozzi, P., Baseggio, O., Bonfà, P., Brunato, D., Car, R., Carnimeo, I., Cavazzoni, C., De Gironcoli, S., Delugas, P., Ferrari Ruffino, F., Ferretti, A.

Quantum ESPRESSO toward the exascale. *The Journal of Chemical Physics*, 152(15), 2020.

[32] Perdew, J. P., Burke, K., Ernzerhof, M. Generalized gradient approximation made simple. *Physical Review Letters*, 77(18): 3865, 1996.

[33] Hamann, D. R. Optimized norm-conserving Vanderbilt pseudopotentials. *Physical Review B—Condensed Matter and Materials Physics*, 88(8): 085117, 2013.

[34] Barone, V., Casarin, M., Forrer, D., Pavone, M., Sambi, M., Vittadini, A. Role and effective treatment of dispersive forces in materials: Polyethylene and graphite crystals as test cases. *Journal of Computational Chemistry*, 30(6): 934–939, 2009.

[35] Onida, G., Reining, L., Rubio, A. Electronic excitations: density-functional versus many-body Green's-function approaches. *Reviews of modern physics*, 74(2): 601, 2002.

[36] Rohlfing, M., Louie, S. G. Electron-hole excitations and optical spectra from first principles. *Physical Review B*, 62(8): 4927, 2000.

[37] Strinati, G. Effects of dynamical screening on resonances at inner-shell thresholds in semiconductors. *Physical Review B*, 29(10): 5718, 1984.

[38] Sangalli, D., Ferretti, A., Miranda, H., Attaccalite, C., Marri, I., Cannuccia, E., Melo, P., Marsili, M., Paleari, F., Marrazzo, A., Prandini, G. Many-body perturbation theory calculations using the yambo code. *Journal of Physics: Condensed Matter*, 31(32): 325902, 2019.

[39] Marini, A., Hogan, C., Grüning, M., Varsano, D. Yambo: an ab initio tool for excited state calculations. *Computer Physics Communications*, 180(8): 1392–1403, 2009.

[40] Thanh Tien, N., Thi Bich Thao, P., Thi Han, N., Khuong Dien, V. Symmetry-driven valleytronics in the single-layer tin chalcogenides SnS and SnSe. *Physical Review B*, 109(15): 155416, 2024.

[41] Guo, G. Y., Lin, J. C. Second-harmonic generation and linear electro-optical coefficients of BN nanotubes. *Physical Review B—Condensed Matter and Materials Physics*, 72(7): 075416, 2005.

[42] Guo, G. Y., Lin, J. C. Systematic ab initio study of the optical properties of BN nanotubes. *Physical Review B—Condensed Matter and Materials Physics*, 71(16): 165402, 2005.

[43] Peng, L., Wang, C., Qian, Q., Bi, C., Wang, S., Huang, Y. Complete Separation of Carriers in the GeS/SnS Lateral Heterostructure by Uniaxial Tensile Strain. *ACS Applied Materials and Interfaces*, 9(46): 40969–40977, 2017.

[44] Kirchhoff, A., Deilmann, T., Krüger, P., Rohlfing, M. Electronic and optical properties of a hexagonal boron nitride monolayer in its pristine form and with point defects from first principles. *Physical Review B*, 106(4): 2022.